Inorg. Chem. **2009**, *48*, 1105−1113

Water−Dichloromethane Interface Controlled Synthesis of Hierarchical Rutile TiO_2 Superstructures and Their Photocatalytic Properties

Changhua Wang,[†,‡,§] Changlu Shao,[†] Yichun Liu,*[,†] and Xinghua Li[†]

Centre for Advanced Optoelectronic Functional Materials Research, Northeast Normal University, Changchun 130024, Key Laboratory of Excited State Processes, Changchun Institute of Optics, Fine Mechanics, and Physics, Chinese Academy of Sciences, Changchun 130033, and Graduate University of Chinese Academy of Science, Beijing 100049, People's Republic of China

Received September 22, 2008

A water−dichloromethane interface is used for synthesis and assembly of rutile TiO_2 nanorods. By hydrothermal treatment of a dichloromethane solution of $TiCl_4$ at the interface of water−dichloromethane, turning to no surfactant or template, hierarchical rutile TiO_2 superstructures are developed. By tuning the molar ratio of reactants r_w (H_2O/$TiCl_4$), the size and shape of the samples significantly change. At a low value of r_w, highly extended, robust, porous, and thick titania film with ordered rutile nanorod bundles are deposited at the interface. At a high value of r_w, powders consisting of hierarchical rutile nanorod spheres together with disordered nanorods are obtained. A rational formation mechanism is proposed on the basis of a range of experiments. The main factors influencing the morphologies of the samples may be attributed to the acidity of the reaction system and the adsorption ability of the precursor nanoparticles to the water−dichloromethane interface. The as-obtained rutile TiO_2 hierarchical superstructures show higher photocatalytic property to decompose methylene blue (MB) dye compared with that of commercial P25, which can be ascribed to the contribution of high surface area and high crystallinity. Other applications, such as solar energy conversion, environmental remediation, and advanced optical/electric nanodevices may also benefit from the unique properties of the hierarchically rutile TiO_2 superstructures.

1. Introduction

Driven by its wide-ranging potential applications in solar cell, water splitting, environment cleanup, white pigments, cosmetics, and so forth, research on nanostructural TiO_2 is rapidly burgeoning over the past three decades.[1−7] Many recent efforts have been focused on the hierarchical assembly of TiO_2 nanoparticles, nanorods, nanotubes, and so forth into ordered complex hierarchical architectures or superstructures due to their advantage of reserving the novel nanometer-scale properties as well as convenience of storing and handling as expected for their micrometer-scale counterparts.[8−12] Although great progress has been achieved on the synthesis approaches for hierarchical architectures, they usually require expensive and even toxic templates or surfactants, high temperature, and a series of complicated procedures. The introduction of templates, surfactants, or other additives into the final products not only increases the production cost but also makes it more difficult to scale-up

* To whom correspondence should be addressed. E-mail: ycliu@nenu.edu.cn; Phone: +86 431 5099168; Fax: +86 431 5684009.
† Northeast Normal University.
‡ Changchun Institute of Optics, Fine Mechanics and Physics, Chinese Academy of Sciences.
§ Graduate University of Chinese Academy of Science.

(1) Asahi, R.; Morikawa, T.; Ohwaki, T.; Aoki, K.; Taga, Y. *Science* **2001**, *293*, 269.
(2) Nakamura, R.; Imanishi, A.; Murakoshi, K.; Nakato, Y. *J. Am. Chem. Soc.* **2003**, *125*, 7443.
(3) Yu, J. C.; Wang, X. C.; Fu, X. Z. *Chem. Mater.* **2004**, *16*, 1523.
(4) Chen, X.; Mao, S. S. *Chem. Rev.* **2007**, *107*, 2891.
(5) Testino, A.; Bellobono, I. R.; Buscaglia, V.; Canevali, C.; D'Arienzo, M.; Polizzi, S.; Scotti, R.; Morazzoni, F. *J. Am. Chem. Soc.* **2007**, *129*, 3564.
(6) Scotti, R.; Bellobono, I. R.; Canevali, C.; Cannas, C.; Catti, M.; D'Arienzo, M.; Musinu, A.; Polizzi, S.; Sommariva, M.; Testino, A.; Morazzoni, F. *Chem. Mater.* **2008**, *20*, 4051.
(7) Nowotny, M. K.; Sheppard, L. R.; Bak, T.; Nowotny, J. *J. Phys. Chem. C* **2008**, *112*, 5275.
(8) Li, H.; Bian, Z.; Zhu, J.; Zhang, D.; Li, G.; Huo, Y.; Li, H.; Lu, Y. *J. Am. Chem. Soc.* **2007**, *129*, 8406.
(9) Liu, L.; Liu, H. J.; Zhao, Y. P.; Wang, Y. Q.; Duan, Y. Q.; Gao, G. D.; Ge, M.; Chen, W. *Environ. Sci. Technol.* **2008**, *42*, 2342.
(10) Yu, J.; Liu, W.; Yu, H. *Cryst. Growth Des.* **2008**, *8*, 930.
(11) Wang, Y.; Zhang, L.; Deng, K.; Chen, X.; Zou, Z. *J. Phys. Chem. C* **2007**, *111*, 2709.
(12) Xu, H.; Jia, F. L.; Ai, Z. H.; Zhang, L. Z. *Cryst. Growth Des.* **2007**, *7*, 1216.

10.1021/ic8018138 CCC: $40.75
Published on Web 01/07/2009

production. Thus, it still remains a significant challenge to develop facile and effective surfactant-free methods for the synthesis and architecture control of TiO_2 hierarchical nanostructures at low temperature.

Besides, nowadays, it is of great importance to use self-assembly to design highly extended self-supporting superstructures with controllable inner-structure from nanostructural building blocks.[13−16] The liquid−liquid (aqueous−organic) soft interface between two immiscible liquids is being proven to offer an important path to assemble nanoparticles, since the nanoparticles are highly mobile and can easily reach equilibrium on self-assembly at the interface.[17−19] Meanwhile, the liquid−liquid interface has also been used to grow two-dimensional films of nanocrystals turning to no substrate. There have been several recent reports on deposition of nanocrystals and thin films at the interface of two essentially immiscible liquids.[16,20,21] In these methods, a metal precursor dissolved in an organic solvent such as toluene is held in contact with an aqueous layer containing, for example, a reducing agent, sulfiding agent, or base. The reaction (reduction, sulfidation, or hydrolysis) proceeds via the ion transport mediated at the interface. The products of these reactions are deposited at the interface typically forming aggregates of nanocrystals or thin films. This simple technique has been shown to yield nanocrystals of metals such as Au, Ag, and Pd, chalcogenides such as CdS and NiS, as well as extended single-crystalline films of CuO and ZnO.[22−25] Following recent successes, this method of deposition at the liquid−liquid interface is emerging as a simple and inexpensive route to growth and assembly of nanocrystals. The process is potentially easily adapted to large area processing with low fabrication cost. Furthermore, unlike other methods that use templates, little or no effort is required to remove the template at the end of deposition.

Motivated by the above results, we further design and synthesize hierarchical nanostructural TiO_2 via hydrothermal treatment of a dichloromethane solution of $TiCl_4$ at the interface of water−dichloromethane. The experimental observations suggest that the morphology, crystals size of the deposits can be varied by altering the molar ratio r_w (H_2O/$TiCl_4$). Especially, at low value of r_w, the products deposited at the interface consist of highly extended, robust, porous, and thick titania film with ordered rutile nanorod bundles. Unlike other traditional thin TiO_2 films which do not yield to optimum photocatalytic activity due to the small amount of crystalline material and not optimum UV light utilization across the film,[26,27] interestingly, the as-obtained thick film in this work has high photocatalytic activity toward decomposing organic dyes. More importantly, the synthetic process has several advantages: (i) the process is a simple, one-step, one-pot procedure; (ii) the process turns to no surfactant or organometallic precursors or ligands; (iii) the process enables one to obtain substrate-free films of materials.

2. Experimental Section

2.1. Preparation of Hierarchical Rutile TiO_2 Superstructures. The interfacial reaction was performed in a 15-mL Teflon-line stainless autoclave. The pipettes and autoclaves were dried before use. In the synthesis, deionized water was slowly injected into 5 mL of a mixture of dichloromethane and $TiCl_4$ in an ice−water bath to form an aqueous/organic interface. The autoclave was stored in a preheated electric oven at 150 °C for 3 h under autogenously pressure and static conditions and then air-cooled to room temperature. At a low value of r_w (e.g., $r_w = 40{:}1$), a thick film that has an opaque appearance was deposited at the interface when opening and unloading the autoclave. The as-synthesized thick film at the interface could be easily clamped out of the autoclave with tweezers or other microhandling tools and then flushed with ethanol and deionized water. At a high value of r_w (e.g., $r_w = 80{:}1$), the products deposited at the interface were white powders. The powders were collected through centrifugation and washed with ethanol and water. All the products were dried in air at 60 °C for 12 h. In this Article, for simplicity, the samples prepared at a molar ratio of reactants of 40 and 80 are denoted as A and B, respectively.

2.2. Characterization. XRD patterns of the samples were recorded on a Rigaku, D/max-2500 X-ray diffractometer. The field emission SEM was performed on a Hitachi S-4800 FESEM field emission scanning electron microscope. High-resolution transmission electron microscopy (HRTEM) is performed with a JEM-3010 electron microscope. UV−vis/DR spectra of the samples were recorded on a Cary 500 UV−vis-NIR spectrophotometer. Raman spectra were recorded on a Jobin-Yvon HR800 instrument with an Ar^+ laser source of 488 nm wavelength in a macroscopic configuration. Nitrogen porosimetry was performed on a Micromeritics ASAP 2010 instrument. Surface areas were calculated using the Brunauer−Emmett−Teller (BET) equation. Pore size distributions were calculated using the Barret−Joyner−Halenda (BJH) model based on a nitrogen desorption isotherm.

2.3. Photocatalytic Test. The photoreactor was designed with an internal light source (50 W high-pressure mercury lamp with main emission wavelength 313 nm and an average light intensity of 2.85 mW cm^{-2}) surrounded by a water-cooling quartz jacket to cool the lamp, where a 100 mL aliquot of the methylene blue (MB) solution with an initial concentration of 20 mg L^{-1} in the presence of TiO_2 solid catalyst (0.1 g). The solution was stirred in the dark for 30 min to obtain a good dispersion and establish adsorption−desorption equilibrium between the organic molecules and the catalyst surface. Decreases in the concentrations of dyes were

(13) Nykypanchuk, D.; Maye, M. M.; van der Lelie, D.; Gang, O. *Nature* **2008**, *451*, 549.
(14) Sun, C. H.; Wang, N. X.; Zhou, S. Y.; Hu, X. J.; Zhou, S. Y.; Chen, P. *Chem. Commun.* **2008**, 3293.
(15) Kim, M.; Jeong, G. H.; Lee, K. Y.; Kwon, K.; Han, S. W. *J. Mater. Chem.* **2008**, *18*, 2208.
(16) Rao, C. N. R.; Kalyanikutty, K. P. *Acc. Chem. Res.* **2008**, *41*, 489.
(17) Lin, Y.; Skaff, H.; Emrick, T.; Dinsmore, A. D.; Russell, T. P. *Science* **2003**, *299*, 226.
(18) Dryfe, R. A. W. *Phys. Chem. Chem. Phys.* **2006**, *8*, 1896.
(19) Böker, A.; He, J.; Emrick, T.; Russell, T. P. *Soft Matter* **2007**, *3*, 1231.
(20) Gautam, U. K.; Ghosh, M.; Rao, C. N. R. *Langmuir* **2004**, *20*, 10775.
(21) Lu, G.; Li, C.; Shi, G. *Chem. Mater.* **2007**, *19*, 3433.
(22) Agrawal, V. V.; Kulkarni, G. U.; Rao, C. N. R. *J. Colloid Interface Sci.* **2008**, *318*, 501.
(23) Rao, C. N. R.; Kulkarni, G. U.; Agrawal, V. V.; Gautam, U. K.; Ghosh, M.; Tumkurkar, U. *J. Colloid Interface Sci.* **2005**, *289*, 305.
(24) Thomas, P. J.; Fan, D.; O'Brien, P. *J. Nanosci. Nanotechnol.* **2007**, *7*, 1689.
(25) Rao, C. N. R.; Kulkarni, G. U.; Thomas, P. J.; Agrawal, V. V.; Saravanan, P. *J. Phys. Chem. B* **2003**, *107*, 7391.
(26) Hosono, E.; Fujihara, S.; Kakiuchi, K.; Imai, H. *J. Am. Chem. Soc.* **2004**, *126*, 7790.
(27) Zhao, Y.; Zhang, X. T.; Zhai, J.; He, J. L.; Jiang, L.; Liu, Z. Y.; Nishimoto, S.; Murakami, T.; Fujishima, A.; Zhu, D. B. *Appl. Catal., B* **2008**, *83*, 24.

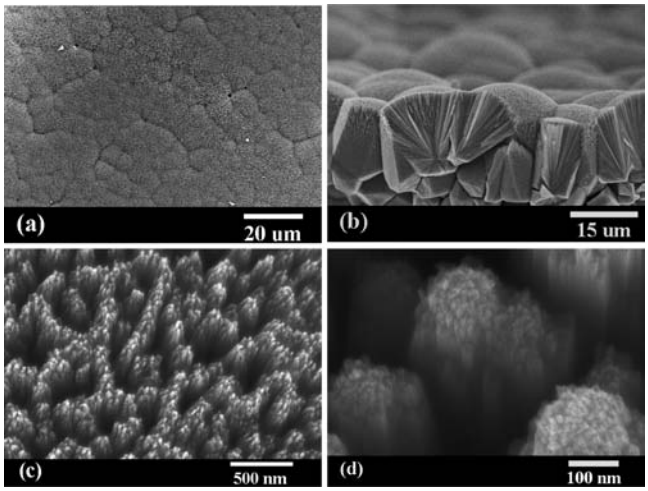

Figure 1. SEM image of sample A: (a) an overall plan view SEM image of the rutile TiO_2 hierarchical structures; (b) cross-section view of the sample; (c,d) high-magnification SEM images of the rutile TiO_2 hierarchical structures.

analyzed by a Cary 500 UV−vis-NIR spectrophotometer at $\lambda =$ 664 nm. At given intervals of illumination, the samples of the reaction solution were taken out and analyzed.

3. Results and Discussion

3.1. Morphology, Crystal Structure. Figure 1a shows an overall plan view SEM image of the representative sample A. The sample displays a flat thick filmlike morphology. The surface of the film is homogeneous, without macrocrack formation, which demonstrates good structural integrity. In a cross section view (Figure 1b), the film thickness is ca. 20 μm. Moreover, it is observed that the film is consisted of many densely packed interconnected spheres. At high magnification (Figure 1c), the film surface exhibits a characteristic porous structure and comprises a large quantity of loosely packed column-shaped nanobundles. The bundles are uniformly distributed and well-aligned to form a hierarchically ordered array. On further close examination, it can be observed that each column-shaped nanobundle comprises tens of neighboring nanorods. Because the closely bundled nanorods are not easily imaged for finer details, an interbundles region is selected where individual nanorods can be observed at high magnification (Figure 1d). The result clearly reveals that diameter of the TiO_2 nanorod is 10 nm.

The microstructure of the as-obtained sample A is further analyzed using TEM and HRTEM. Figure 2 shows TEM and HRTEM images of typical sample A. The TEM result (Figure 2a) reveals that the sample consists of nanobundles composed of radially aligned nanorods of around 10 nm in diameter. In addition, slitlike nanopores are observed within the spaces between adjacent nanorods. The HRTEM result (Figure 2b) clearly shows that rutile nanorods are highly crystallized. The distance between the adjacent lattice fringes can be assigned to the interplaner distance of rutile TiO_2 (110), which is $d_{110} = 0.325$ nm. The nanorods therefore grow in the [001] direction. The preferential growth along this direction is arising from the unique crystal structure of rutile. It is known that rutile has 4_2 screw axes along the

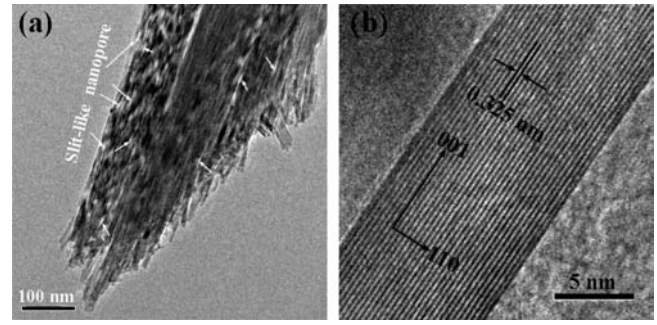

Figure 2. (a) TEM image of representative sample A; (b) HRTEM image of a nanorod of TiO_2.

crystallographic *c*-axis.[28,29] The screw structure will promotes the crystal growth along this direction, leading to a crystal morphology dominated by the {110} faces.

We further explored the influence of different reaction conditions on the formation of hierarchical TiO_2 superstructure. It was found that r_w can significantly affect the size and shape of the products. If r_w is decreased to 20:1 while keeping other reaction conditions the same, the as-obtained product also shows a two-dimensional filmlike feature (Figure 3a). Likewise, the film is composed of spherical aggregates, and these spherical structures have no obvious region between each other. The magnified image (Figure 3b) reveals that the spherical aggregates are assembled by many loosely packed cone-shaped nanobundles. The nanobundles are assembled by several nanorods with diameters about 20 nm (Figure 3c). However, when r_w is increased to 80:1, very differently, the as-obtained product consists of some round spheres with a diameter of about 700 nm and numerous randomly packed nanorods (Figure 3d). The high-magnification SEM image in Figure 3e exhibits detailed information about the sphere architecture, which is composed of nanorods with a diameter less than 10 nm. The nanorods are radially oriented to its center and self-organized into a spherical-like assembly. Figure 3f shows the high-magnification SEM image of randomly packed nanorods. The diameter is also less than 10 nm. Consequently, different hierarchical rutile TiO_2 superstructures are obtained at the interface of water−dichloromethane by simply tuning the molar ratio of reactants.

XRD measurement is used to identify the phase of the hierarchical TiO_2 superstructures. TiO_2 has two main phases, anatase, which can be kinetically favored over rutile, the thermodynamically stable phase. Figure 4 shows the XRD patterns of typical film sample A and powder sample B, respectively. It can be seen that, for both samples, there are six typical peaks with 2θ values of 27.52°, 36.20°, 41.44°, 54.48°, 63.24°, and 69.56°, corresponding to (110), (101), (111), (211), (002), and (301) crystal planes of pure rutile TiO_2, respectively (JCPDS, No. 77-0441). No characteristic peaks of impurities such as anatase TiO_2 are detected. Further analysis shows that, with decreasing r_w from 80:1 to 40:1, XRD peak intensities of rutile TiO_2 steadily become stronger

(28) Howard, W. J. *Crystal Chemistry and Refractivity*; Cambridge University Press: Cambridge, U.K., 1988.
(29) Cheng, H. M.; Ma, J. M.; Zhao, Z. G.; Qi, L. M. *Chem. Mater.* **1995**, *7*, 663.

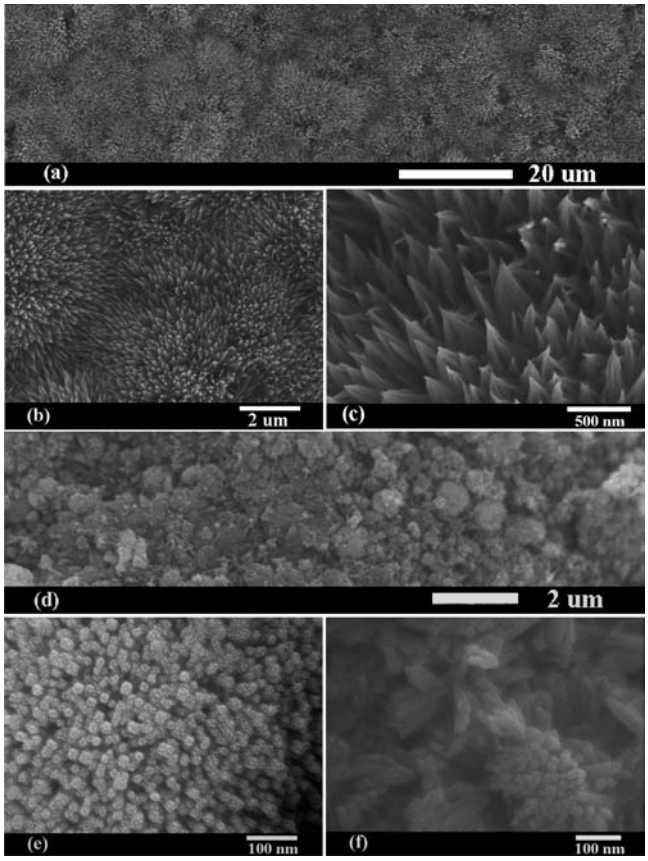

Figure 3. SEM image of sample prepared at different value of r_w: (a) an overall plan view SEM image of the rutile TiO_2 hierarchical structures at a value of $r_w = 20$; (b,c) high-magnification SEM images of the rutile TiO_2 hierarchical structures; (d) SEM image of the rutile TiO_2 hierarchical structures at a value of $r_w = 80$; (e) high-magnification SEM images of an individual rutile TiO_2 nanorods sphere; (f) high-magnification SEM images of the randomly packed rutile TiO_2 nanorods.

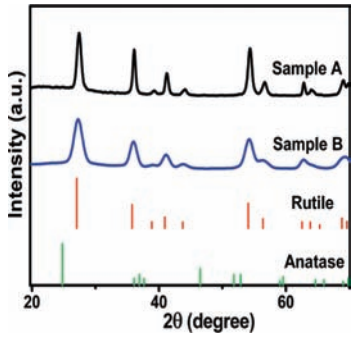

Figure 4. XRD patterns of samples A and B. The vertical lines indicate the position and intensity of anatase and rutile reflections.

and the width of XRD diffraction peaks becomes slightly narrower, indicating the formation of greater TiO_2 crystallites and an enhancement of crystallization, which is in agreement with the SEM results above.

Raman scattering has proven to be a versatile technique for characterizing nanostructured materials. Figure 5 shows the Raman spectra of samples A and B as well as that of bulk rutile and anatase. For sample A, the Raman spectra give peaks broader than those of bulk rutile. The clearly visible Raman bands at 606, 433, and 255 cm^{-1} are characteristic vibrations of rutile. The band near 606 cm^{-1} is identified as the A1g mode, and the band near 433 cm^{-1}

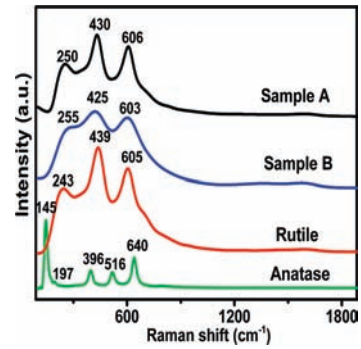

Figure 5. Raman spectra of samples A and B.

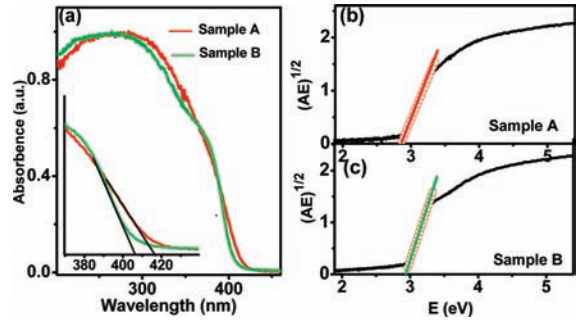

Figure 6. (a) UV−vis absorption spectra of samples A and B; (b,c) determination of indirect interband transition energies for samples A and B.

is identified as the Eg mode. The broadband near 255 cm^{-1} is a second-order phonon.[30,31] No additional Raman bands assigned to anatase are observed, which further confirms the single rutile phase feature of the TiO_2 samples. For sample B, the A1g mode (603 cm^{-1}), Eg mode (425 cm^{-1}), as well as second phonon line (255 cm^{-1}) are also detected. Additionally, the results show some general trends in the behavior of the peak's positions (Eg and A1g modes) for both samples when comparing with that of bulk rutile. That is, the rutile Eg mode shows a red shift (shift from 439 to 430 cm^{-1} for sample A; shift from 439 to 425 cm^{-1} for sample B), and the rutile A1g mode shows a random shift (shift from 605 to 603 cm^{-1} for sample A; shift from 605 to 606 cm^{-1} for sample B), which can be due to the effect of grain size for nanocrystalline rutile TiO_2.[32]

3.2. Optical Properties of Rutile TiO_2 Hierarchical Structures. The optical band gaps of the rutile TiO_2 samples are studied by means of UV−vis optical absorbance spectra. Figure 6 shows UV−vis absorption spectra of the typical rutile TiO_2 samples, from which the optical absorption edges are found to be 416.1 nm for sample A and 406.6 nm for sample B, corresponding to their optical bandgaps of 2.98 and 3.05 eV, respectively. In other words, a blue shift in the band gap adsorption edge of TiO_2 is observed from sample A to B, due to the quantum-size effect. TiO_2 is known as an indirect semiconductor; the band gap energies can also be estimated from a plot of $(\alpha h\nu)^{1/2}$ versus photon energy ($h\nu$).

(30) Chaves, A.; Katiyan., K. S.; Porto, S. P. S. *Phys. Rev.* **1974**, *10*, 3522.
(31) Zhang, Y. H.; Chan, C. K.; Porter, J. F.; Guo, W. *J. Mater. Res.* **1998**, *13*, 2602.
(32) Mazza, T.; Barborini, E.; Piseri, P.; Milani, P.; Cattaneo, D.; Bassi, A. L.; Bottani, C. E.; Ducati, C. *Phys. Rev. B* **2007**, *75*, 045416.

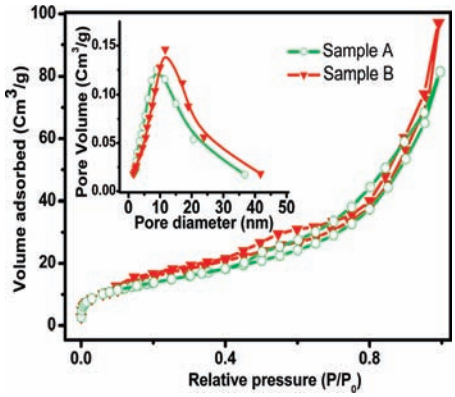

Figure 7. Nitrogen adsorption−desorption isotherm and pore size distribution curve (inset) of samples A and B.

The intercept of the tangent to the plot will give a good approximation of the indirect band gap energies of the samples. The relationship between the absorption coefficient (α) and incident photon energy ($h\nu$) can be written as $\alpha = B_i(h\nu - Eg)^2/h\nu$, in which B_i is the absorption constant for indirect transitions. As absorbance (A) is proportional to the absorption coefficient (α), here, α is substituted by A. Plots of $(Ah\nu)^{1/2}$ versus ($h\nu$) from the spectral data of Figure 6a are presented in Figure 6b−c. Extrapolating the linear part of the curve for samples A and B gives an indirect band gap of 2.86 and 2.92 eV, respectively. Once again, the blue shift of the optical band gap is confirmed. This is in reasonable agreement with the SEM, XRD, and Raman results above.

3.3. Textural Structure of the Hierarchical Structures. The porous structures of the resulting rutile TiO_2 samples are studied by nitrogen sorption. Figure 7 presents the nitrogen adsorption−desorption isotherms and BJH pore size distribution curve (inset) of samples A and B. Both samples show the type IV isotherms with type H3 hysteresis loops according to BDDT classification, which suggests the presence of mesopores (2−50 nm) in the product. The isotherms with type H3 hysteresis loops are associated with slitlike nanopores, which is in well coincidence with the TEM results. The corresponding pore size distributions show that the mean mesopore diameter of samples A and B are 8.9 and 11.6 nm, respectively. The mesopores are derived from fine intra-aggregated pores formed between intra-agglomerated primary rutile nanorods. The determined BET specific surface areas of samples A and B are 51.0 and 78.9 m^2/g, respectively.

3.4. Formation Mechanism. Combining the structural characterization results above, we conclude that different hierarchical rutile TiO_2 superstructures can be obtained at the interface of water−dichloromethane by tuning the molar ratio of reactants. The difference in morphology synthesized at different values of r_w can be summarized as follows: (i) the diameter of rutile nanorods decreases as the value of r_w increases; (ii) the nanorods tend to agglomerate to form nanobundles at a lower value of r_w; (iii) the sample obtained at a lower value of r_w shows thick film morphology consisting of ordered nanorods whereas the sample obtained at a higher value of r_w shows powder morphology consisting of hierarchical nanorods spheres and disordered nanorods.

The overall reaction occurred at the interface can be described as

$$TiCl_4 + 2H_2O = TiO_2(\text{rutile}) + 4HCl$$

At the very beginning, TiO_2 nanoparticles are formed via forced hydrolysis of $TiCl_4$ at the interface. Indeed, there is strong evidence that, at the early stage of hydrothermal preparation of rutile nanorods, precursor nanoparticles are initially formed.[12,14,26,33−35] From the hydrolytic equations of the $TiCl_4$ solution, it is known that, when the amount of $TiCl_4$ added is kept unchanged, the lower molar ratio of reactants (r_w), the lower concentration of H_2O in the $TiCl_4$ solution, the stronger the acidity of the reaction system. It is well-reported that the pH of the reaction system has a significant effect on the rutile nanocrystals growth.[36,37] In this experiment, the excess of H^+ ions may suppress the hydrolytic process of the $TiCl_4$ solution and results in a low reaction rate; thus, fewer rutile precursor nanoparticles are formed in the highly concentrated acidic solution. Moreover, some of the rutile precursor nanoparticles may be dissolved rapidly in concentrated acidic media, and only relatively large and stable rutile nanoparticles remain in the concentrated acidic solution. In other words, the higher the value of r_w, the smaller the size of the TiO_2 precursor nanoparticles. Further crystal growth mainly proceeds via oriented coalescence of the primary small nanoparticles at high autoclaving temperature and after prolonged autoclaving, giving rise to rutile nanorods. With this regard, the reason that the diameter of the rutile TiO_2 nanorods decreases with an increasing value of r_w can be ascribed to the difference of the size of the precursor TiO_2 nanoparticles.

The acidity of the reaction medium should also be a critical factor to the nanorods agglomeration during hydrolysis of an acidic $TiCl_4$ aqueous solution.[38] The surface properties of TiO_2 can be changed by protonation as follows: $TiO_2 + nH^+ = TiO_2H_n^{n+}$ under highly acidic conditions. The agglomeration of rutile TiO_2 nanorods is promoted, which is attributed to hydrogen bonding among the protonated rutile nanorods. In this case, the preformed nanorods can attach to each other in an oriented fashion to decrease the surface energy of the system and result in the formation of products with bundle structures. In a weakly acidic medium, however, the coordinated water molecules suppress the agglomeration among the freshly formed rutile nanorods, so leading to separated nanorod growth. Therefore, the nanorods trend to agglomerate to form nanobundles at lower r_w values.

To further understand the growth mechanism of the TiO_2 hierarchical structures on the interface of water−dichloromethane, we perform a series of experiments to explore the formation process. The first experiment is carried out in the absence

(33) Yang, S. W.; Gao, L. *Chem. Lett.* **2005**, *34*, 7.
(34) Dessombz, A.; Chiche, D.; Davidson, P.; Panine, P.; Chanéac, C.; Jolivethave, J. P. *J. Am. Chem. Soc.* **2007**, *129*, 5904.
(35) Bai, X. L.; Xie, B.; Pan, N.; Wang, X. P.; Wang, H. Q. *J. Solid State Chem.* **2008**, *181*, 450.
(36) Zhang, Q. H.; Gao, L. *Langmuir* **2003**, *19*, 967.
(37) Yin, H.; Wada, Y.; Kitamura, T.; Sumida, T.; Hasegawa, Y.; Yanagida, S. *J. Mater. Chem.* **2002**, *12*, 378.
(38) Bahnemann, D.; Henglein, A.; Spanhel, L. *Faraday Discuss. Soc.* **1984**, *78*, 151.

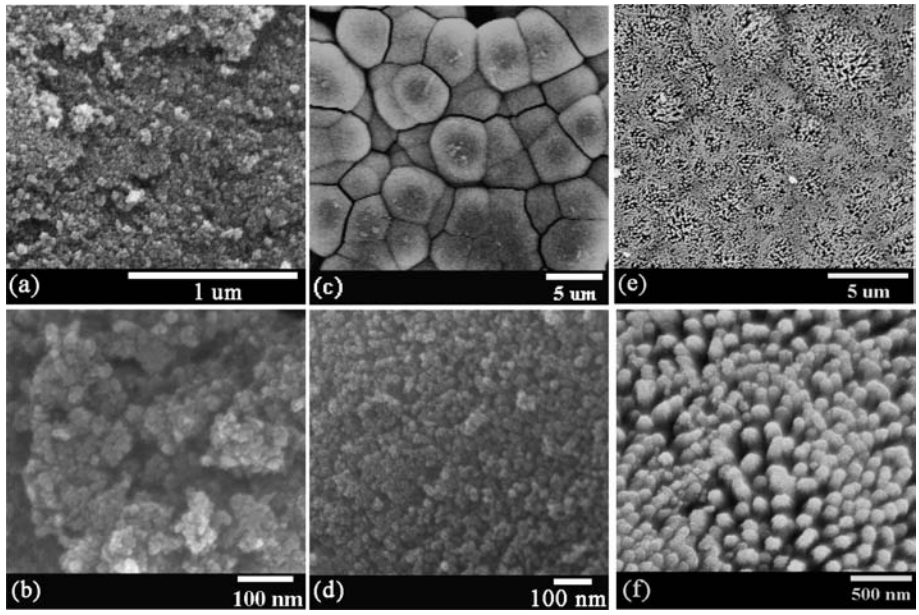

Figure 8. SEM image of the samples prepared at a molar ratio of $H_2O/TiCl_4 = 40$ under hydrothermal treatment for (a,b) 20 min; (c,d) 40 min; (e,f) 60 min.

of a liquid−liquid interface to know if the liquid−liquid interface plays an important role in the formation of TiO_2 hierarchical superstructures (see the Supporting Information). In this case, a great deal of white precipitates is generated in the bottom of the autoclave. The products are collected, dried, and used for SEM analysis. It is found that only randomly orientated nanorods are obtained (See Figures S1 of the Supporting Information). Therefore, we believe that the interface of water−dichloromethane plays a crucial role in the formation of rutile TiO_2 hierarchical structures. The second time-dependent experiment is carried out by collecting products at different reaction stages when $r_w = 40:1$. Figure 8 shows a series of typical intermediate morphologies corresponding to the growth process evolution of TiO_2 superstructures. Initially, small-sized nanoparticles are formed at the liquid−liquid interface as shown in Figure 8a. The magnified image reveals that the diameter of nanoparticles ranges from 10 to 20 nm (Figure 8b). After 40 min, these nanoparticles are then self-assembled into spheres (Figure 8c−d). The spheres are interconnected with adjacent spheres, and the diameter of the sphere is in micrometer scale. By prolonging the reaction time to 60 min, complex structures being spread across the water−dichloromethane interface are formed by continuous aggregative assembly of spheres (Figure 8e). High magnification (Figure 8f) reveals that precursor nanoparticles diminish; instead, numerous nanobundle arrays take on at the surface of the sphere. Accordingly, the possible whole process may include three steps, which just correspond to the practical reaction process: (i) formation of precursor nanoparticles. At the beginning, since $TiCl_4$ tends to react with water vigorously, lots of TiO_2 nanoparticles are formed rapidly at increased temperature. It was revealed that the adsorption of particles to the liquid−liquid interface is thermodynamically favorable.[17] Thus, the thermal activated TiO_2 nanoparticles can be trapped at the water−dichloromethane interface in order to reduce interfacial energy. (ii) Formation of hierarchical TiO_2 nanoparticles spheres. As the reaction proceeds, spherical emulsions with diameters of several micrometers are formed at the water−dichloromethane interface because of extreme conditions during hydrothermal treatment. Meanwhile, the TiO_2 nanoparticles assembled at the interface stabilize the emulsion, which, in turn, effectively stabilize the liquid−liquid interfaces. Since the concentration of TiO_2 nanoparticles at the interface is high, the aggregation can easily take place. Thus, the nanoparticles may be tightly packed in emulsions and/or stick to the interfacial surface of the emulsions. Hence, hierarchical TiO_2 spheres composed of nanoparticles are formed. Driven by the reduction of electrostatic repulsion and the increase of van der Waals interactions between each sphere, these spheres are inclined to aggregate at the interface.[17,39] In fact, the interface has been considered in some detail by colloid scientists, who have known for many years that nanoparticles can be used to stabilize liquid−liquid interfaces, leading to so-called spherical Pickering (or Ramsden) emulsions.[40,41] Usually, the diameter of the emulsion is in micrometer scale and the size of the nanoparticles ranges from 2 to 20 nm in diameter. In simple terms, the nanoparticle stabilizes the interface because it minimizes the extent of interactions between the two immiscible liquids; nanoparticles can thus become strongly adsorbed at the liquid−liquid interface.[17,42,43] In this regard, it is reasonable that the precursor nanoparticles whose diameters fall in the range 10−20 nm can stabilize the emulsion at the interface. (iii) Growth of rutile nanorods. The precursor nanoparticles undergo further growth into nanorods in the acidic medium

(39) Reincke, F.; Hickey, S. G.; Kegel, W. K.; Vanmaekelbergh, D. *Angew. Chem., Int. Ed.* **2004**, *43*, 458.
(40) Pickering, S. U. *J. Chem. Soc. Trans.* **1907**, *91*, 2001.
(41) Ramsden, W. *Proc. Royal Soc. London Ser. A* **1903**, *72*, 156.
(42) Binks, B. P. *Curr. Opin. Colloid Interface Sci.* **2002**, *7*, 21.
(43) Aveyard, A.; Binks, B. P.; Clint, J. H. *Adv. Colloid Interface Sci.* **2003**, *100*, 503.

under hydrothermal treatment. By owing to the crystallization happening in the space-limited sphere, the product obtained at last at the interface is composed of spheres consisting of ordered nanorods.

However, one question is still present here: why are the free-standing films formed at lower values of r_w rather than high r_w? This may be due to the difference in the adsorption ability to the interface of the precursor nanoparticles. Theoretically, interfacial assembly of nanoparticles is dictated by a minimization of the Helmholtz free energy.[17] Placement of one nanoparticle at an interface will decrease the entropy by about k_B (the Boltzmann constant). Consequently, the energy change, ΔE, must be negative to reduce the total free energy. The three contributions to the interfacial energy arise from the particle−oil interface ($\gamma_{P/O}$), the particle−water interface ($\gamma_{P/W}$), and the oil−water interface ($\gamma_{O/W}$). ΔE, due to the assembly of a single particle at the oil−water interface, is given by

$$\Delta E = -\frac{\pi R^2}{\gamma_{O/W}} \times [\gamma_{O/W} - (\gamma_{P/W} - \gamma_{P/O})]^2$$

where R is the effective radius of the nanoparticle. For microscopic particles, the decrease in total free energy is much larger than thermal energy (a few k_BT) leading to an effective confinement of large colloids to the interface. Nanoscopic particles however are confined to the interface by an energy reduction comparable to thermal energy. Therefore, the thermally activated escape of small particles takes place more often than for larger ones. Following these theoretical thoughts, in combination with the characterization results above, we speculate the reason for the formation of powders consisting of spheres and randomly packed nanorods at the interface at higher values of r_w. At the beginning of the reaction, smaller sized nanoparticles are formed compared with that of precursor nanoparticles formed at lower values of r_w. These nanoparticles have weaker adsorption ability to the interface due to their smaller size, which in turn suppress their continuous aggregative assembly at the interface. As demonstrated by previous work, [44] the further growth of precursor TiO_2 nanoparticles is remarkably influenced by the acidic conditions, which may result in the preferred growth of rutile along the *c*-axis and form nanorods. Moreover, Oliver et al.[45] calculated the specific surface energies of rutile TiO_2 based on atomistic simulation and claimed the surface energies of {100}, {221}, {011}, and {110} were 2.08, 2.02, 1.85, and 1.78 J m^{-2}, respectively. The structure of rutile consisted of chains of TiO_6 octahedra, in which each octahedron shared a pair of opposite edges in the {001} plane,along which titanium−oxygen octahedra shared one edge forming octahedral filaments. Accordingly, the {110} plane is the most stable plane of rutile TiO_2; the rodlike nanocrystal is formed due to the rutile chain type fast growth along the [001]-axis. The rutile TiO_2 nanorods obtained in our case show a high aspect ratio, which agrees well with

(44) Zheng, Y. Q.; Shi, E. W.; Chen, Z. Z.; Li, W. J.; Hu, X. F. *J. Mater. Chem.* **2001**, *11*, 1547.
(45) Oliver, P. M.; Watson, G. M.; Kelsey, E. T.; Stephen, C. P. *J. Mater. Chem.* **1997**, *7*, 563.

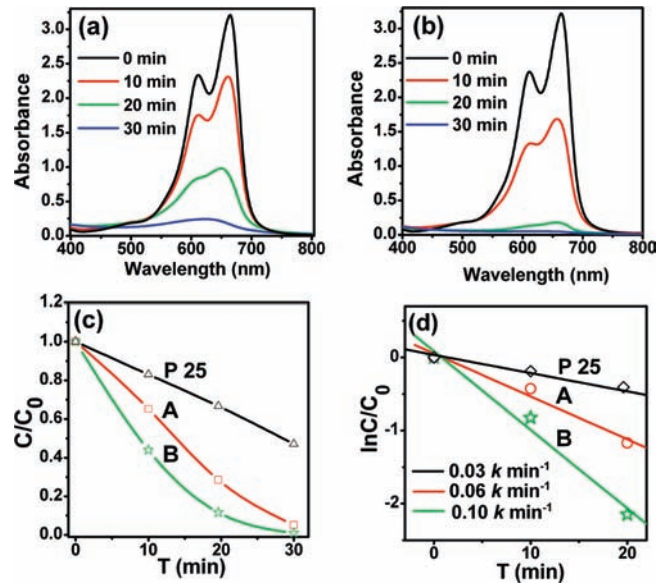

Figure 9. (a) Time-dependent adsorption spectra of MB solutions in the presence of sample A; (b) time-dependent adsorption spectra of MB solutions in the presence of sample B; (c) time course of the photodegradation of MB on UV light irradiated catalysts; (d) first-order linear transform $\ln(C_0/C) = f(t)$ for different catalysts.

the theoretical calculation and previously demonstrated results. Thus, besides the nanorods crystallized at the liquid−liquid interface, many nanorods crystallize in the aqueous phase. As the reaction proceeds, the length and diameter of the nanorods both increase and last randomly sedimentate at the interface. Therefore, powders containing a minority of spheres together with lots of disordered nanorods are obtained at a higher value of r_w. The possible mechanism of the self-assembly of rutile TiO_2 hierarchical superstructures at the liquid−liquid interface at different values of r_w can be illustrated in Figure 10.

3.5. Photocatalytic Activity. To demonstrate the photoactivity of the present hierarchical structural rutile TiO_2 samples for the degradation of organic pollutants, we have carried out the experiments of the photocatalytic degradation of MB as a test reaction. The photocatalytic control experiments indicate that there is no appreciable degradation of MB over TiO_2 either in the absence of UV irradiation or in the absence of the catalyst (not shown). However, the absorption peaks corresponding to MB at 664 nm diminish gradually as the exposure time is extended in the presence of different TiO_2 samples under UV light. Figure 9a shows the absorption spectra of an aqueous solution of MB in the presence of sample A irradiated by UV light at different periods of time. The absorption peak at 664 nm rapidly decreases in intensity with the prolonging of the exposure time: 92% MB was degraded after only 30 min. No new absorption peaks appear in the whole spectra. Further comparative experiments are carried out in the presence of powder photocatalyst including sample B as well as photocatalyst P25 (Degussa P25, 80% anatase and 20% rutile; specific surface area 50 m^2g^{-1} and a mean particle size of 30 nm). Experiments are performed using an identical amount of powder as film sample A. Figure 9b shows that, for sample B, the absorption peak of MB disappears almost

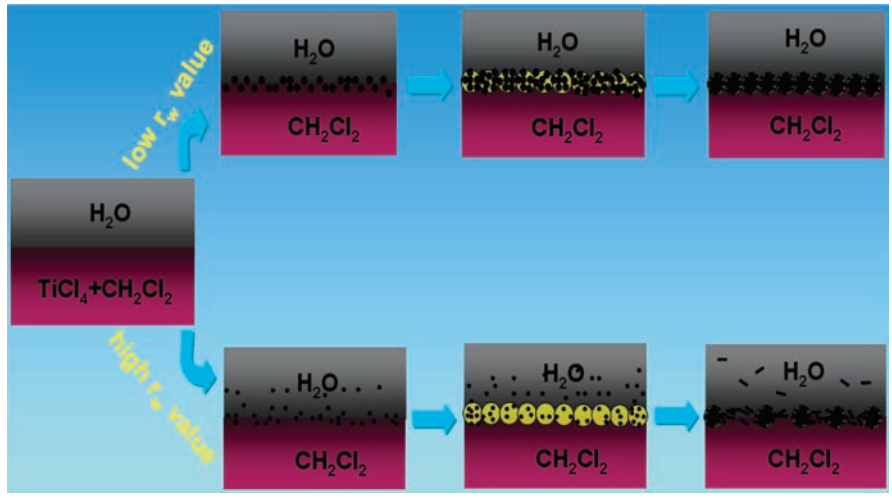

Figure 10. Proposed mechanism of the self-assembly of the rutile TiO_2 superstructure at the liquid−liquid interface.

completely after 30 min. Figure 9c demonstrates that the degradation rate of both samples A and B are higher than P25 in which 53% MB still exists after 30 min irradiation.

For a better comparison of the photocatalytic efficiency of different catalysts, kinetic analysis of degradation and mineralization of MB in water are employed. The kinetic linear simulation curves of MB photocatalytic degradation over different catalysts demonstrate that the above degradation reactions follow a Langmuir−Hinshelwood apparent first-order kinetics model due to the low initial concentrations of the reactants. The explanation is described below:

$$r = -\mathrm{d}C/\mathrm{d}t = kKC/(1 + KC) \quad (1)$$

where r is the degradation rate of the reactant (mg/(L min)), C is the concentration of the reactant (mg/L), t is the UV−light illumination time, k is the reaction rate constant (mg/(L min)), and K is the adsorption coefficient of the reactant (L/mg). When the initial concentration (C_0) is very low ($C_0 = 20$ mg/L for MB in the present experiment) eq 1 can be simplified to an apparent first-order model

$$\ln(C_0/C) = kKt = k_{app}t \quad (2)$$

where k_{app} is the apparent first-order rate constant (min^{-1}). The determined k_{app} for different catalysts are summarized in Figure 9d. The photocatalytic reactivity order is B > A > P25, which is well-consistent with the activity studies above.

Generally, the difference of photocatalytic activity can be explained in terms of large surface area, small crystallite size, and high crystallinity. Meanwhile, the effects of these factors are interdependent. First, large surface area is likely to exhibit better photocatalytic activity because a large surface area provides more active sites for adsorbing MB solution. So, the sample with higher surface area possesses higher activity; for example, the activity order is B (78.9 m^2/g) > A (51.0 m^2/g). Second, the degree of crystallization is also a significant factor determining photocatalytic activity. It has been proven that photoactivity and crystallinity are inextricably linked and the photocatalytic activity increases with increases in the crystallinity.[46,47] Indeed, it has been reported that the rutile titania with a small surface area and high crystallinity (i.e., low lattice defect density) exhibits a high level of photocatalytic activity for oxygen liberation. Therefore, the activity difference between A and B can be attributed to the balance between specific surface area and crystallinity. Third, it has also been commonly accepted that smaller crystallite size corresponds to more powerful redox ability because smaller crystallite size induces a larger band gap that causes the rate of electron-hole recombination to be slower.[48] This can be well-reflected in the difference of activity that B (2.92 eV) > A (2.86 eV). Last, it must be pointed out that, in the design of the photochemical reactor and actual photocatalytic application, especially for mineralizing liquid pollutant, film photocatalysts (sample A) are more important than those of powder (sample B and P25) and suspension photocatalysts because the annoying process to recycle the fine powders from the reaction mixture can be avoided.

4. Conclusion

The present work demonstrates that a water−dichloromethane interface can be exploited as a medium to prepare hierarchical rutile TiO_2 superstructures. The morphology of the TiO_2 hierarchical superstructures can be perfectly manipulated by simply controlling the molar ratio of reactants. A free-standing thick film with ordered nanorods can be obtained at lower molar ratio of reactants whereas, at a higher molar ratio of reactants, powders composed of hierarchical nanorods spheres and disordered nanorods are obtained. The key steps of this process involve formation of precursor nanoparticles and Pickering emulsion and the growth of rutile TiO_2 nanorods. The reason for the variation of the morphologies of the samples may be ascribed to the acidity of the reaction system and the adsorption ability of the precursor nanoparicles to the water−dichloromethane interface. High photocatalytic activity of the as-synthesized samples in the degradation of MB has been demonstrated. Among the as-

(46) Peng, T.; Zhao, D.; Dai, K.; Shi, W.; Hirao, K. *J. Phys. Chem. B* **2005**, *109*, 4947.
(47) Ohtani, B.; Ogawa, Y.; Nishimoto, S. I. *J. Phys. Chem. B* **1997**, *101*, 3746.
(48) Yu, J. C.; Zhang, L.; Yu., J. *Chem. Mater.* **2002**, *14*, 4647.

synthesized samples, the thick films are expected to find actual application for water decontamination due to its high activity and facile recovery and reuse. The key issue for large scale applications is the development of synthesis methods that produce a hierarchically structured photocatalyst with large surface areas at low cost. The employed synthesis route in this work is surfactant-free and template-free and thus not only decreases the production cost but also makes it easier to scale up production. It may also be general for other hierarchical inorganic oxide superstructures.

Acknowledgment. This work is supported by National High Technology Research and Development Program of China (2006AA03Z311), Cultivation Found of the Key Scientific and Technical Innovation Project (Grant No. 704017), Ministry of Education of China, National Natural Science Foundation of China (Grant No. 60576040 and 50572014), Program for New Century Excellent Talents in University (NCET-05-0322).

Supporting Information Available: Synthesis and SEM image of rutile TiO_2 in the absence of a liquid−liquid interface. This material is available free of charge via the Internet at http://pubs.acs.org.

IC8018138